UC Santa Cruz

UC Santa Cruz Previously Published Works

Title

High-efficiency in situ resonant inelastic x-ray scattering (iRIXS) endstation at the Advanced Light Source

Permalink

Journal

ISSN

Authors

Qiao, Ruimin
Li, Qinghao
Zhuo, Zengqing
et al.

Publication Date

DOI

Peer reviewed

High-efficiency *in situ* resonant inelastic x-ray scattering (iRIXS) endstation at the Advanced Light Source

Ruimin Qiao,[1] Qinghao Li,[1,2] Zengqing Zhuo,[1,3] Shawn Sallis,[1,4] Oliver Fuchs,[5]
Monika Blum,[6] Lothar Weinhardt,[6,7,8] Clemens Heske,[6,7,8] John Pepper,[1] Michael Jones,[1]
Adam Brown,[9] Adrian Spucces,[9] Ken Chow,[9] Brian Smith,[9] Per-Anders Glans,[1]
Yanxue Chen,[2] Shishen Yan,[2] Feng Pan,[3] Louis F. J. Piper,[4] Jonathan Denlinger,[1]
Jinghua Guo,[1] Zahid Hussain,[1] Yi-De Chuang,[1,a)] and Wanli Yang[1,a)]

[1]*Advanced Light Source, Lawrence Berkeley National Laboratory, 1 Cyclotron Road, Berkeley, California 94720, USA*
[2]*School of Physics, National Key Laboratory of Crystal Materials, Shandong University, Jinan 250100, People's Republic of China*
[3]*School of Advanced Materials, Peking University Shenzhen Graduate School, Shenzhen 518055, People's Republic of China*
[4]*Department of Materials Science and Engineering, Binghamton University, Binghamton, New York 13902, USA*
[5]*Universität Würzburg, Experimentelle Physik 7, 97074 Würzburg, Germany*
[6]*Department of Chemistry and Biochemistry, University of Nevada, Las Vegas (UNLV), Las Vegas, Nevada 89154-4003, USA*
[7]*Institute for Photon Science and Synchrotron Radiation (IPS), Karlsruhe Institute of Technology (KIT), 76344 Eggenstein-Leopoldshafen, Germany*
[8]*Institute for Chemical Technology and Polymer Chemistry (ITCP), Karlsruhe Institute of Technology (KIT), 76128 Karlsruhe, Germany*
[9]*Engineering Division, Lawrence Berkeley National Laboratory, Berkeley, California 94720, USA*

An endstation with two high-efficiency soft x-ray spectrographs was developed at Beamline 8.0.1 of the Advanced Light Source, Lawrence Berkeley National Laboratory. The endstation is capable of performing soft x-ray absorption spectroscopy, emission spectroscopy, and, in particular, resonant inelastic soft x-ray scattering (RIXS). Two slit-less variable line-spacing grating spectrographs are installed at different detection geometries. The endstation covers the photon energy range from 80 to 1500 eV. For studying transition-metal oxides, the large detection energy window allows a simultaneous collection of x-ray emission spectra with energies ranging from the O K-edge to the Ni L-edge without moving any mechanical components. The record-high efficiency enables the recording of comprehensive two-dimensional RIXS maps with good statistics within a short acquisition time. By virtue of the large energy window and high throughput of the spectrographs, partial fluorescence yield and inverse partial fluorescence yield signals could be obtained for all transition metal L-edges including Mn. Moreover, the different geometries of these two spectrographs (parallel and perpendicular to the horizontal polarization of the beamline) provide contrasts in RIXS features with two different momentum transfers. *Published by AIP Publishing.* [http://dx.doi.org/10.1063/1.4977592]

I. INTRODUCTION

Third-generation synchrotron-based resonant inelastic soft x-ray scattering (RIXS) has become a powerful technique for studying both fundamental physics and chemical systems.[1–4] RIXS can be viewed as a combination of coherent absorption and emission processes.[5,6] By varying the excitation photon energy and studying the evolution of x-ray emission spectra, RIXS can provide detailed insights into the electronic structure, electronic correlations, as well as a multitude of dynamic processes. Moreover, RIXS is explicitly a bulk-sensitive probe and can be employed for probing solid, liquid, and gaseous samples.[7–10] However, due to the very low fluorescence yield in the soft x-ray regime, RIXS experiments often require high incident photon flux

to become feasible, which is one of the reasons why RIXS became practical only with the advent of high-brightness third-generation synchrotron radiation sources. The soft x-ray fluorescence (SXF) endstation at Beamline 8.0.1 and the AXIS endstation at Beamline 7.0.1 with Rowland-circle spectrometers at the Advanced Light Source (ALS) were the first generation of endstations dedicated to soft x-ray RIXS spectroscopy.[11,12] Over the past two decades, considerable efforts have been made to improve the RIXS performance in terms of detection efficiency[13] and energy resolving power.[14] These new spectrograph designs utilize variable line-spacing (VLS) gratings to achieve much improved detection efficiency, energy resolution, and flexibility in general.[15–24] The resulting high energy resolution RIXS spectrographs, such as SAXES operated at the ADRESS beamline of the Swiss Light Source[14,21] and the SXE spectrometer at BL07LSU in Spring-8, Japan,[24] have been extensively used in fundamental physics studies.[3]

While the energy resolution of RIXS has been greatly improved through these instrumentation developments, and studies of low energy excitations in highly correlated physics have been enabled and demonstrated extensively, RIXS remains a photon hungry technique and is limited by its low detection efficiency for studying many technological materials, especially those suffering radiation damage effects and/or under *in situ/operando* conditions. A low-energy (up to 650 eV) high-throughput VLS spectrograph was commissioned at the ALS in 2007,[13] which allows the collection of entire RIXS "maps" (maps of emission intensity as a function of both emission and excitation energies).[13,25] The enhanced RIXS detection efficiency of this spectrograph has demonstrated great potentials in studying materials for biological and energy applications under *in situ* conditions.[7,26,27] However, because many technologically important materials are based on *3d* transition-metal (TM) compounds, extending the energy range of high throughput spectrographs to cover all *3d* transition-metal *L*-edges has become a pressing demand for understanding and optimizing the properties of such materials.

We have therefore developed the high-throughput *in situ* resonant inelastic x-ray scattering (iRIXS) endstation at the ALS. The iRIXS endstation features two slit-less VLS spectrographs with different priorities on efficiencies, resolving powers, and detection geometries, both featuring a wide operation energy range up to 1500 eV. These two spectrographs use the same focused synchrotron beam spot as the source, which is produced by a dedicated bendable refocus soft x-ray mirror assembly just upstream of iRIXS. The system incorporates the *in situ* sample environment reported previously.[28,29] This article presents the design and performance of the iRIXS endstation, with examples of soft x-ray absorption spectroscopy (sXAS) collected in four different modes, soft x-ray emission spectroscopy (XES), and large energy-range RIXS maps of transition-metal *L*-edges and the carbon *K*-edge.

II. THE iRIXS ENDSTATION

A CAD drawing of the iRIXS endstation at Beamline 8.0.1 of the ALS is shown in Fig. 1. iRIXS has two high-throughput VLS soft x-ray spectrographs mounted at different angles relative to the incident x-ray beam. The spectrograph that offers higher resolution (hrRIXS) is mounted 90° to the incident photon beam direction, and the high-throughput spectrograph (htRIXS) is installed at back-scattering geometry with an angle of 160° relative to the incident photon direction. The two spectrographs with different parameters and detection geometries offer the opportunities for various sXAS, XES, and RIXS experiments, which will be discussed in more detail.

Both spectrographs use the same refocused beam spot on the sample as the source (≤25 μm in the vertical direction), which is produced by a bendable mirror located just 0.6 m upstream of iRIXS.[30,31] The gold-coated refocus mirror with dimensions of 200 mm (L) × 20 mm (W) × 7 mm (H) is fabricated from GlidCop AL-15. This mirror has leaf-spring benders on both ends that can be adjusted by motorized linear feedthroughs to change the curvature to compensate the
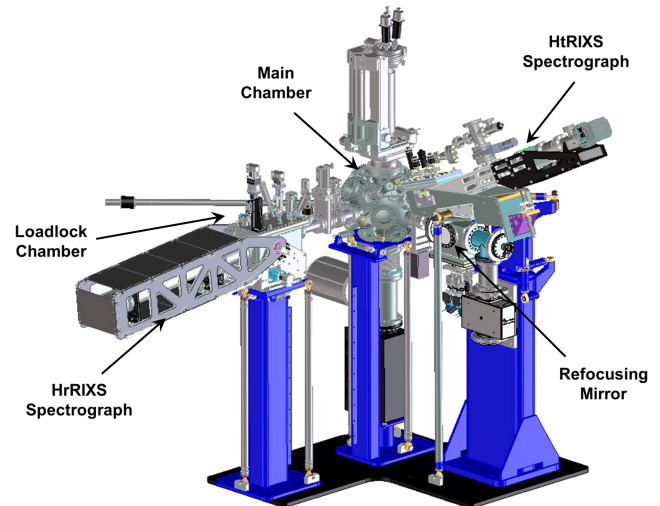

FIG. 1. A CAD drawing showing the iRIXS endstation at Beamline 8.0.1 at the Advanced Light Source (ALS), Lawrence Berkeley National Laboratory (LBNL).

moving source point (beamline exit slit). The mirror assembly can also be pitched to change the deflection angle for beam-based optimization. All motions are encoded with optical encoders for positional references. Besides these two VLS spectrographs, the characterization chamber is also equipped with standard sXAS detectors (a channeltron and a multi-channel plate detector). The ultra-high vacuum manipulator inside the characterization chamber has three translational and three rotational degrees of freedom. The temperature of the sample stage can be varied between 20 and 700 K. The sample stage is compatible with *in situ* sample environment setups that have been demonstrated previously.[28,29] A separate load-lock chamber with an independent pumping system is used for fast sample loading without compromising the vacuum of the characterization chamber. The direct photon flux from the beamline monochromator is 10^{13} photons per second focused to a 100 μm × 100 μm spot.[11] In our RIXS measurement condition in this manuscript, the photon flux on the sample is about 10^{12} photons per second after the refocus optics at the energy range of 500–1000 eV (using different monochromator gratings).

The schematic of the slit-less VLS spectrograph is shown in Fig. 2. It consists of three major elements: a spherical pre-mirror, a plane VLS grating, and a CCD detector. This
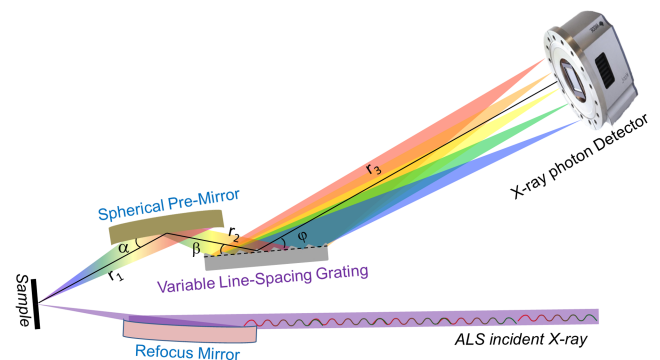

FIG. 2. Schematic illustration of the optical design of a slit-less VLS spectrograph.

TABLE I. Optical parameters of the htRIXS spectrograph that includes two sets of spherical mirrors and VLS plane gratings in order to cover both the low energy (80-550 eV) and high energy (450-1500 eV) range. The thickness of the mirrors is 12 mm and the thickness of the VLS gratings is 15 mm. The optical parameters of the hrRIXS spectrograph are also presented for a direct comparison.

		HtRIXS		HrRIXS[33]
		Low energy	High energy	
Mirror:	Dimensions	20×80 mm^2	20×80 mm^2	90×90 mm^2
	Distance (r_1)	400 mm	399.36 mm	900 mm
	Angle (α)	4.3°	2.412°	2°
	Radius of curvature	8420.01 mm	14982.2 mm	29472 mm
Grating:	Dimensions	20×120 mm^2	20×120 mm^2	90×100 mm^2
	Distance (r_2)	105 mm	105 mm	100 mm
	Distance (r_3)	1392.1 mm	1392.1 mm	1100 mm
	Angle (β)	2.2694°	1.1459°	1.5°
	Angle (φ)	Adjustable	Adjustable	Adjustable
	Blaze angle	2.0307°	1.2134°	N/A
	Central groove density	$a_0 = 600$ lines/mm	$a_0 = 900$ lines/mm	$a_0 = 2400$ lines/mm
	VLS parameters	$a_1 = 0.859031$ lines/mm^2	$a_1 = 1.29154$ lines/mm^2	$a_1 = 4.35259$ lines/mm^2
		$a_2 = 4.08416 \times 10^{-4}$ lines/mm^3	$a_2 = 8.84197 \times 10^{-4}$ lines/mm^3	$a_2 = 0.005757$ lines/mm^3
		$a_3 = -4.52801 \times 10^{-8}$ lines/mm^4	$a_3 = 3.62557 \times 10^{-7}$ lines/mm^4	$a_3 = 0.000007$ lines/mm^4
	Rule density (lines/mm)		$n(x) = a_0 + a_1 x^1 + a_2 x^2 + a_3 x^3$	
Detector:	Dimensions		27.6×27.6 mm^2	
	Pixel dimensions		13.5×13.5 μm^2	
Throughput:	Acceptance angle	12.4×14.5 mrad^2	6.3×14.5 mrad^2	2.6×14.5 mrad^2
	Resolving power (1st order energy)	1938–1228 (115 eV–174 eV)	1142–854 (438 eV–877 eV)	8000–3000 (200 eV–1000 eV)

configuration has advantages towards improving the spectrograph efficiency by generating a focal plane normal to the optical axis, allowing the use of the CCD detector in normal incidence geometry to yield optimal quantum efficiency.[20,32] In addition, the refocused x-ray beam spot on the sample is used as the source, which alleviates the need for an entrance slit. This slit-less operation greatly improves the acceptance angle of the spectrograph and increases the throughput without compromising the energy resolution.

The most important optical design parameters for both htRIXS and hrRIXS spectrographs are summarized in Table I, while more details of the hrRIXS (replica of the modular x-ray spectrograph for the qRIXS endstation at the ALS) can be found in Ref. 33. For htRIXS, several parameters were designed as a compromise that improves the RIXS detection efficiency while maintaining adequate energy resolution. The htRIXS spectrograph is designed to work in inner (positive) diffraction order geometry. It has two sets of spherical mirrors and plane VLS gratings for covering the low energy (LE) (80-550 eV) and high energy (HE) (450-1500 eV) ranges, respectively. The inner order operation leads to high efficiency and a large energy window on the CCD detector. The grazing incident angle of the mirror, 4.3° for LE and 2.4° for HE, is optimized to maximize the merit function $M(\alpha) = \alpha \cdot R^2(\alpha)$, where α is the grazing incidence angle that is related to the photon collection solid angle and $R(\alpha)$ is the angle-dependent reflectivity (reflections from the mirror and the grating). Note that a larger grazing incidence angle than the ideal value is selected for the HE design to simplify the process of aligning the optics. A low central ruling density of the VLS gratings, 600 lines/mm for LE and 900 lines/mm for HE, is selected

to improve the overall grating efficiency. To increase the collection solid angle, the optics are mounted as close to the source point as possible. The distance from the mirror center to the sample spot at the center of the iRIXS characterization chamber is about 400 mm. Because of the different angles for the LE and HE optics, the two spherical mirrors are offset and mounted with two different rotational axes (Fig. 3). This leads to a different distance from the source (sample) to the mirrors, namely, 400.00 mm for LE and 399.36 mm for
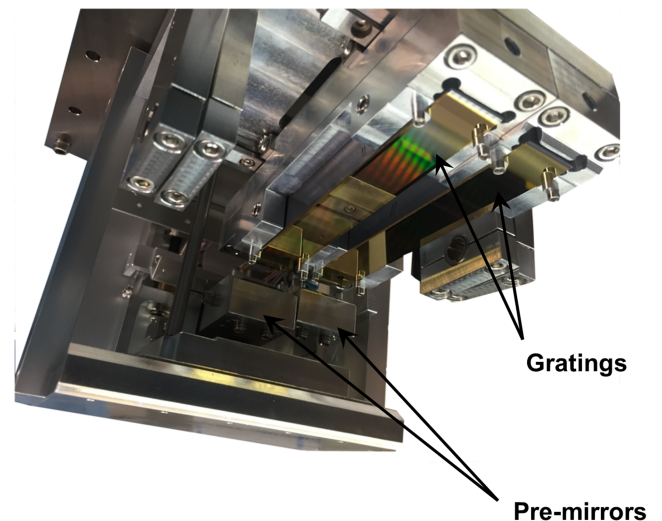

FIG. 3. A picture showing the internal construction of the htRIXS spectrograph that includes two sets of spherical mirrors and VLS plane gratings. The two mirrors are offset to compensate the different beam paths for low- and high-energy photons.
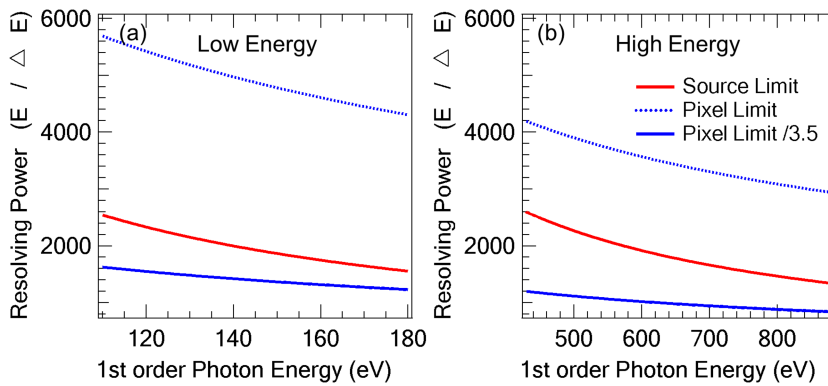
FIG. 4. The source limit and the CCD pixel limit of the resolving power as a function of the 1st order photon energy for the htRIXS spectrograph. The beam spot is 25 μm and the pixel size of the CCD detector is 13.5 μm. A minimum of 3.5 pixels is considered to define a peak. The resolving power of the spectrograph is limited by the CCD pixel size.

HE. The CCD detector is rotatable around the grating center (angle φ) to change the detector energy window. The distance from the CCD to the grating (r_3) can be adjusted for calibration purposes. The angles of mirror and gratings can be changed separately using linear feedthroughs mounted on the lid of the optics chamber, and the angles are recorded by in-vacuum linear variable differential transformers (LVDTs). During the normal operations, these angles will be kept constant. The calculated resolving power for both low energy and high energy optical sets of the hrRIXS spectrograph is shown in Fig. 4. In this figure, both source limit and detector pixel limit are plotted as a function of the first order photon energy. The beam spot is 25 μm and the pixel size of the CCD detector is 13.5 μm. A minimum of 3.5 pixels is considered to define a peak. It is shown that the resolving power of the hrRIXS spectrograph is limited by the CCD pixel size.

III. XES AND RIXS MAP OF LiNi$_{0.33}$Co$_{0.33}$Mn$_{0.33}$O$_2$ (NCM)

To demonstrate the potential of the iRIXS endstation, with its large energy window and high throughput, for soft x-ray emission spectroscopy, Fig. 5 shows the XES spectra of LiNi$_{0.33}$Co$_{0.33}$Mn$_{0.33}$O$_2$ (NCM) with 900 eV excitation

FIG. 5. XES spectra of LiNi$_{0.33}$Co$_{0.33}$Mn$_{0.33}$O$_2$ (NCM) collected using two VLS spectrographs (excitation energy of 900 eV). The acquisition time (from top to bottom) is 10 and 60 s with htRIXS and 60 and 300 s with hrRIXS, respectively. For easy comparison, the intensity of the 10 s and 300 s spectra has been rescaled by the factor of 6 and 1/5, respectively. The relatively stronger noise level in the 60S hrRIXS spectrum could be due to the difference on the CCD readout noise and/or cosmic ray reduction process.

energy. NCM is one of the promising electrode materials for energy storage that is under scrutiny by both academic and industrial researchers.[34] Additionally, NCM is a multi-element system with equal amounts of three different transition metals. Here, we use NCM as a model system and study pristine NCM powder that is free of the widely known surface Mn^{2+} phase.[35] For Fig. 5, four XES spectra were taken using both spectrographs in iRIXS with different acquisition times, from top to bottom: 10 and 60 s with htRIXS and 60 and 300 s with hrRIXS, respectively. Both spectrographs can cover the photon energy range from the O K-edge (540 eV) to the Ni L-edge (850 eV) without any mechanical movement. All XES spectra exhibit strong peaks from the O 2p-1s transition and the Mn, Co, and Ni 3d-2p transitions. These XES spectra represent the occupied electronic states near the Fermi level, in particular, O 2p and Mn, Co, and Ni 3d states, which are responsible for the physical and chemical properties of NCM. Interestingly, due to the large energy window of the spectrograph, the 3s-2p transitions could be observed simultaneously for the transition-metals (Fig. 5).

Since all transitions were recorded simultaneously without moving any mechanical component in the spectrographs, the difference in the relative intensities is intrinsic to the sample under study and is related to the elemental composition, the photon attenuation lengths, the efficiency of the spectrometer for the given energy, and the fluorescence yield of the different transitions.[36] The intensity behavior of these peaks is thus a complex function of a variety of parameters. Nevertheless, by using reference materials, tabulated attenuation lengths,[37] and a self-consistent quantification (taking self-absorption effects into account), a (semi-)quantitative picture of the elemental composition in the surface-near bulk can be obtained. Such insights can be favorably combined with more surface-sensitive information obtained by x-ray photoelectron spectroscopy (XPS) and can furthermore also be derived under *in situ* or operando conditions (when employing suitable cells and membranes). Note that based on the intensity contrast between the two spectrographs as shown in Fig. 5, the htRIXS spectrograph has the efficiency roughly two times higher than that of the hrRIXS spectrograph in this energy range.

The high throughput of the spectrographs makes it practical to collect RIXS maps of transition-metal L-edges with fine excitation energy steps and within a reasonably short time. Additionally, the large energy window of the spectrograph allows us to obtain two different types of absorption
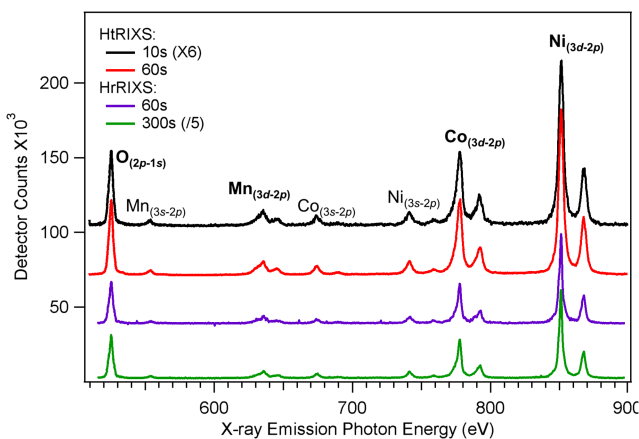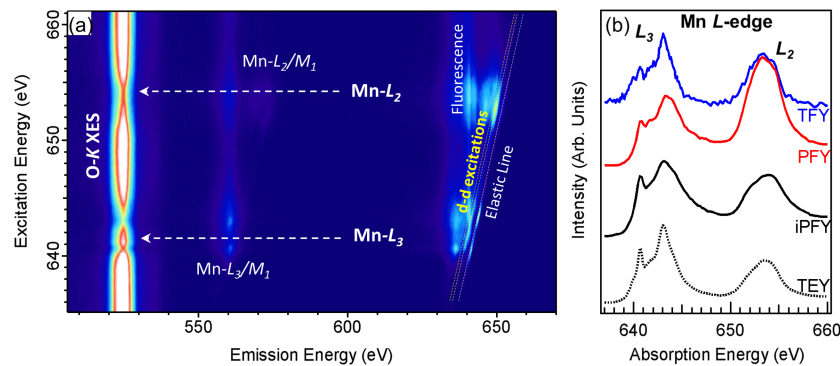
FIG. 6. (a) 2D RIXS map of LiNi$_{0.33}$Co$_{0.33}$Mn$_{0.33}$O$_2$ (NCM) displayed against the excitation (vertical axis) and emission (horizontal axis) photon energy. The map was collected using the hrRIXS spectrograph while varying the excitation x-ray photon energy across the Mn $L_{2,3}$-edge. (b) Four different types of x-ray absorption spectra of NCM at the Mn $L_{2,3}$-edge: total fluorescence yield (TFY), partial fluorescence yield (PFY), inverse partial fluorescence yield (iPFY), and total electron yield (TEY). Among them, PFY and iPFY were obtained by integrating the 2D RIXS map in different ranges of emission photon energy.

spectra, partial fluorescence yield (PFY) *and* inverse partial fluorescence yield (iPFY),[31,32] which makes use of the multiple emission features in the RIXS map with a large energy window, for example, the Mn $L_{2,3}$-edge RIXS and O K-edge XES as elaborated below.

Figs. 6–8 display the 2D RIXS maps of NCM with excitation photon energies at Mn $L_{2,3}$-edge, Co L_3-edge, and Ni L_3-edge, respectively. The Mn $L_{2,3}$-edge map (Fig. 6) was taken in about 3 h, and the Co and Ni L_3-edge maps (Figs. 7 and 8) were each collected in about 2 h. As shown in Fig. 6(a), the 2D RIXS map at the Mn $L_{2,3}$-edge (vertical axis) consists of three main regions. These are (from high to low emission energy) the Mn $L_{2,3}$-edge RIXS, the Mn-$L_{2,3}/M_1$ XES, and the O-K XES. One can see that the Mn $L_{2,3}$-edge RIXS signals consist of energy-loss features (Mn $3d$-$3d$ orbital excitations) that are parallel to the elastic line, as well as "normal" fluorescence features that have fixed emission energies (vertical stripes in the map). Note that the interpretation of transition-metal RIXS maps can provide abundant insights into the chemical valence, symmetry, coordination, spin states, charge transfer, and electronic excitations of the material.[2]

Moreover, the Mn $L_{2,3}$-edge PFY sXAS spectrum can be extracted by integrating the intensity in this RIXS map

between emission energies of 620 and 660 eV, and the iPFY spectrum is the inverse of the integration of the O-K XES window (between 510 and 540 eV).[31,32] Both Mn $L_{2,3}$-edge PFY and iPFY spectra are displayed, together with the total electron yield (TEY) and total fluorescence yield (TFY) spectra collected simultaneously through other absorption signal channels, in Fig. 6(b). TFY spectra generally suffer from self-absorption and saturation effects, which can cause distortions of the spectral lineshape.[38,39] In contrast, the iPFY is a truly bulk probe without such distortions. We would like to point out that silicon drift detectors (SDDs), typically used for PFY and iPFY measurements, have an energy resolution of about 100 eV that is too poor for resolving elements with close emission energies, e.g., Mn and O as in the present case.[31,32] The VLS spectrographs presented here have a much higher energy resolution, so that the iPFY and PFY of the Mn $L_{2,3}$-edge could be reliably extracted from the RIXS map as a "byproduct" without any problem. For RIXS maps at the Co and Ni L_3-edges, we cut out the Co and Ni emission regions (Figs. 7(b) and 8(b)) and the O-K XES "responses" (Figs. 7(a) and 8(a)). In all transition-metal RIXS maps, energy loss features parallel to the elastic lines and the normal emission features at fixed emission energy can be seen and distinguished. Again,
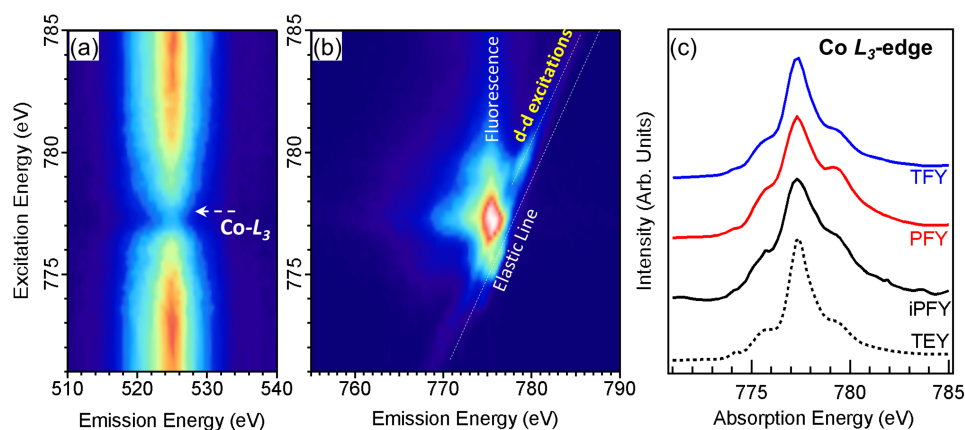

FIG. 7. 2D RIXS maps of LiNi$_{0.33}$Co$_{0.33}$Mn$_{0.33}$O$_2$ (NCM) with the emission photon energies at the O K-edge (a) and Co L_3-edge (b), respectively. The two 2D maps were collected simultaneously using the hrRIXS spectrograph (same as Fig. 6) while varying the excitation x-ray photon energy across the Co L_3-edge. (c) Four different x-ray absorption spectra of NCM at the Co L_3-edge, including TFY, PFY, iPFY, and TEY. PFY and iPFY were obtained by integrating the 2D RIXS map in different emission photon energy ranges.
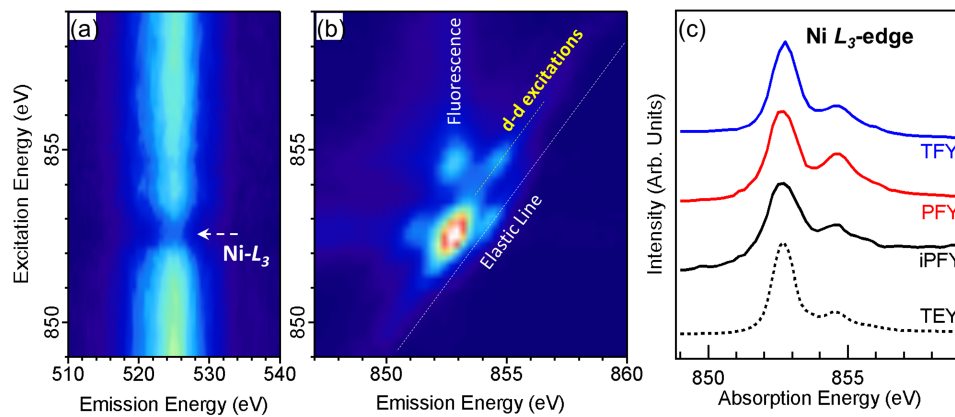
FIG. 8. 2D RIXS maps of LiNi$_{0.33}$Co$_{0.33}$Mn$_{0.33}$O$_2$ (NCM) with the emission photon energies at the O K-edge (a) and the Ni L_3-edge (b), respectively. The two 2D maps were collected simultaneously using the hrRIXS spectrograph (same as Fig. 6) while varying the excitation x-ray photon energy across the Ni L_3-edge. (c) Four different x-ray absorption spectra of NCM at the Ni L_3-edge, including TFY, PFY, iPFY, and TEY. PFY and iPFY were obtained by integrating the 2D RIXS map in different emission photon energy ranges.

different types of sXAS spectra are extracted from the associated RIXS maps and plotted in Figs. 7(c) and 8(c).

IV. RIXS OF HOPG WITH DIFFERENT DETECTION GEOMETRY

Figs. 9 and 10 show the RIXS maps of HOPG at the carbon K-edge, measured with the hrRIXS and htRIXS spectrographs, respectively. In both figures, the sXAS spectra are displayed in panel (a) and the RIXS maps are displayed in two different formats: the 2D image (panel (b)) and the stacked RIXS spectra with different excitation photon energies (panel (c)). The spectra collected with excitation energies of 285.3 eV (π^*), 291.6 eV (σ^* exciton), and 292.8 eV (σ^*) are highlighted black in panel (c), as well as indicated by the dashed lines in panels (a) and (b). The incident x-ray beam is 45° relative to the sample surface normal, while the emitted x-ray photons are detected at 90° (Fig. 9) and 160° (Fig. 10) relative to the incident photon beam.

Each RIXS map consists of 60 RIXS spectra with excitation energies spanning the C K-edge (horizontal cut). In this energy range, the htRIXS spectrograph has significantly higher efficiency than the hrRIXS spectrograph: the acquisition time for each emission spectrum is 3 min for hrRIXS and 10 s for htRIXS. Compared with the htRIXS data, the hrRIXS result

shows significantly improved energy resolution. The resolution of the hrRIXS spectrograph is limited by the physical resolution limit of the CCD pixels, which is about 13.5 μm.[40] In addition, compared with the old SXF spectrometer of the same beamline, the efficiency of the htRIXS spectrograph at the C-K edge is increased by 100 times, and its resolution is about 1.5 times higher (Table I).[41]

The dispersive features observed in these RIXS maps are in agreement with previous results of HOPG.[13,41] These features arise from interband transitions in graphite.[42] Here we focus on the contrast between the data collected with hrRIXS and htRIXS spectrographs at different detection geometries. First, the relative intensity of the elastic peak is much higher in Fig. 9 than in Fig. 10, which is likely due to the specular geometry in the measurement. Second, the inelastic feature as indicated by the white arrows at 284-285 eV excitation energy (vertical axis) and 282-283 eV emission energy (horizontal axis) corresponds to the critical "Dirac cone" at the K-point of the Brillouin zone of HOPG,[41,42] which is also the central topic of recent studies on graphene and topological insulators.[43] Compared with Fig. 9, which is generally consistent with the previous observations in the same detection geometry,[41] this critical RIXS feature is much enhanced in Fig. 10 and, in particular, has a very different shape. While the feature in Fig. 10 appears to be parallel to the elastic line, the feature
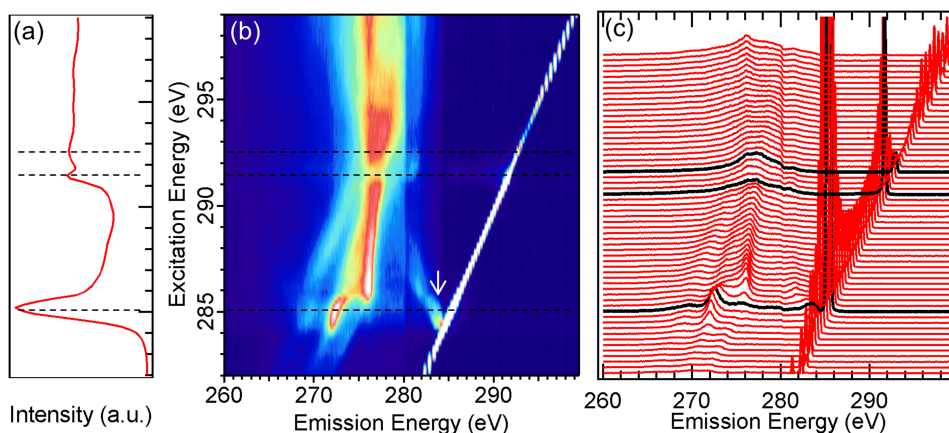

FIG. 9. (a) Carbon K-edge soft x-ray absorption spectrum (sXAS) and ((b) and (c)) RIXS map of HOPG collected using the hrRIXS spectrograph. The incident x-ray is 45° relative to the surface normal and the emitted x-rays are detected at 90° from the incident beam. The emission spectra with excitation energies of 285.3 eV (π^*), 291.6 eV (σ^* exciton), and 292.8 eV (σ^*) are highlighted black in panel (c) and denoted by black dashed lines in panels (a) and (b).
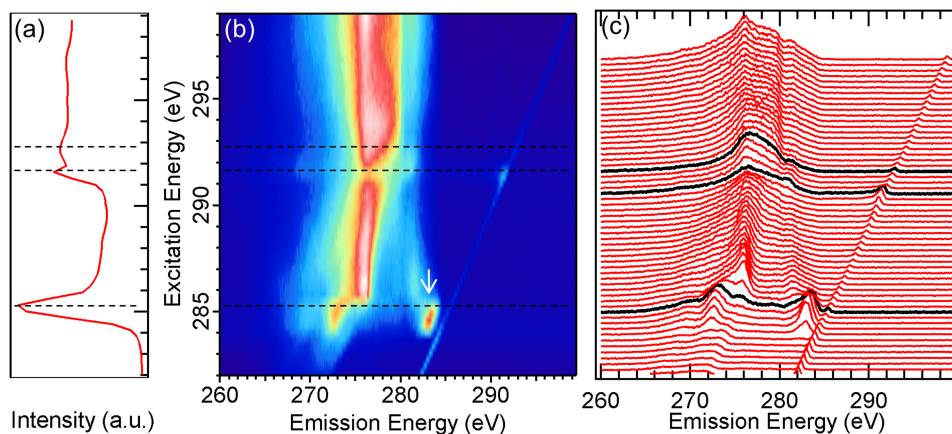
FIG. 10. Carbon *K*-edge sXAS (a) and RIXS map ((b) and (c)) of HOPG collected using the htRIXS spectrograph. The incident x-ray is 45° relative to the surface normal and the emitted x-ray is detected at 160° from the incident beam. The emission spectra with excitation energies of 285.3 eV (π^*), 291.6 eV ($\sigma*$ exciton), and 292.8 eV (σ^*) are highlighted black in panel (c) and denoted by black dashed lines in panels (a) and (b).

in Fig. 9 disperses in the opposite direction, i.e., *towards* the elastic line for decreasing excitation energies. While the latter effect can be assigned to dispersion in a (ground state) band structure description,[11] the former suggests an interpretation in a Raman-type description: the energy separation between the feature and the elastic line (1.9 eV) can be associated with a characteristic energy loss, such as a band gap in a region of k-space different from the *K* point. We suggest that this difference is due to the different momentum transfer between the incoming and outgoing photons for the hrRIXS and the htRIXS spectrograph geometries.[3,42] The detailed and theoretical interpretation of the RIXS maps is obviously not in the scope of this instrumentation article, but we would like to note that the data contrast of the model HOPG system here demonstrates the capability of the iRIXS endstation to tackle the critical electronic states through RIXS with different detection geometries.

V. CONCLUSION

We have described the design and performance of the new iRIXS endstation at Beamline 8.0.1 of the ALS. The endstation features two high-efficiency VLS spectrographs that are dedicated for soft x-ray RIXS experiments. They cover a wide energy range (from 80 to 1500 eV) that gives rise to new experimental opportunities. For example, both spectrographs allow the collection of emission spectra (without any mechanical motion) that cover the range from the O *K*-edge to the Ni *L*-edge (500–900 eV). This opens up the opportunity for a fast and (semi-)quantitative analysis of a large variety of technological materials (such as transition metal oxides). In particular, such studies are now possible in suitably designed *in situ* and *operando* cells.

Combining the continuously adjustable photon energy from the synchrotron light source with the high-efficiency, wide-energy-range x-ray spectrographs, we are now able to collect detailed RIXS maps of all 3*d*-transition-metal *L*-edges covering the full absorption-edge energy range within a reasonably short time. Here, we have presented the 2D RIXS maps of the three transition metals in $LiNi_{0.33}Co_{0.33}Mn_{0.33}O_2$, a battery electrode compound. In addition to the well-distinguished *d-d* excitations and the fluorescence decay of valence states in the transition-metal RIXS data, PFY and iPFY spectra were obtained simultaneously from the RIXS map by virtue of the

large energy window of the spectrograph detector. While it is not our intention to compare the energy resolution with that of the conventional SDD, we would like to mention that the high efficiency RIXS provides the opportunities for collecting iPFY data of TMs with features too broad to be distinguished with the SDD, for example, the Mn L-edge iPFY of oxides as shown in this manuscript. Moreover, the two spectrographs are mounted at different geometries relative to the incident photon beam, which leads to different momentum transfers for the RIXS spectra collected by these two spectrographs. We show that an interesting contrast on the critical Dirac cone feature of the HOPG is revealed by comparing the RIXS maps collected with these two spectrographs. In general, we conclude that the iRIXS system at the ALS is a unique RIXS experimental endstation with ultra-high detection efficiency, wide detection energy window, and two specific detection geometries for studying both the fundamental physics and application-related properties of modern material systems.

[1]Special issue of J. Electron Spectrosc. Relat. Phenom., edited by J. Nordgren, **110-111**, 1–364 (2000).
[2]A. Kotani and S. Shin, Rev. Mod. Phys. **73**(1), 203–246 (2001).
[3]L. J. P. Ament, M. van Veenendaal, T. P. Devereaux, J. P. Hill, and J. van den Brink, Rev. Mod. Phys. **83**(2), 705 (2011).

[4] P. Wernet, K. Kunnus, I. Josefsson, I. Rajkovic, W. Quevedo, M. Beye, S. Schreck, S. Grubel, M. Scholz, D. Nordlund, W. Zhang, R. W. Hartsock, W. F. Schlotter, J. J. Turner, B. Kennedy, F. Hennies, F. M. F. de Groot, K. J. Gaffney, S. Techert, M. Odelius, and A. Fohlisch, Nature **520**(7545), 78–81 (2015).

[5] J.-E. Rubensson, J. Lüning, S. Eisebitt, and W. Eberhardt, Appl. Phys. A **65**(2), 91–96 (1997).

[6] J.-E. Rubensson, J. Electron Spectrosc. Relat. Phenom. **110–111**, 135–151 (2000).

[7] Y. L. Jeyachandran, F. Meyer, S. Nagarajan, A. Benkert, M. Bär, M. Blum, W. Yang, F. Reinert, C. Heske, L. Weinhardt, and M. Zharnikov, J. Phys. Chem. Lett. **5**(23), 4143–4148 (2014).

[8] Y.-S. Liu, P.-A. Glans, C.-H. Chuang, M. Kapilashrami, and J. Guo, J. Electron Spectrosc. Relat. Phenom. **200**, 282–292 (2015).

[9] A. Benkert, M. Blum, F. Meyer, R. G. Wilks, W. Yang, M. Bär, F. Reinert, C. Heske, and L. Weinhardt, Rev. Sci. Instrum. **85**(1), 015119 (2014).

[10] M. Blum, L. Weinhardt, O. Fuchs, M. Bar, Y. Zhang, M. Weigand, S. Krause, S. Pookpanratana, T. Hofmann, W. Yang, J. D. Denlinger, E. Umbach, and C. Heske, Rev. Sci. Instrum. **80**(12), 123102–123106 (2009).

[11] J. J. Jia, T. A. Callcott, J. Yurkas, A. W. Ellis, F. J. Himpsel, M. G. Samant, J. Stohr, D. L. Ederer, J. A. Carlisle, E. A. Hudson, L. J. Terminello, D. K. Shuh, and R. C. C. Perera, Rev. Sci. Instrum. **66**(2), 1394–1397 (1995).

[12] J. Nordgren and J. Guo, J. Electron Spectrosc. Relat. Phenom. **110–111**, 1–13 (2000).

[13] O. Fuchs, L. Weinhardt, M. Blum, M. Weigand, E. Umbach, M. Bar, C. Heske, J. Denlinger, Y. D. Chuang, W. McKinney, Z. Hussain, E. Gullikson, M. Jones, P. Batson, B. Nelles, and R. Follath, Rev. Sci. Instrum. **80**(6), 063103 (2009).

[14] V. N. Strocov, T. Schmitt, U. Flechsig, T. Schmidt, A. Imhof, Q. Chen, J. Raabe, R. Betemps, D. Zimoch, J. Krempasky, X. Wang, M. Grioni, A. Piazzalunga, and L. Patthey, J. Synchrotron Radiat. **17**(5), 631–643 (2010).

[15] Z. Yin, H. B. Peters, U. Hahn, M. Agåker, A. Hage, R. Reininger, F. Siewert, J. Nordgren, J. Viefhaus, and S. Techert, Rev. Sci. Instrum. **86**(9), 093109 (2015).

[16] T. Warwick, Y.-D. Chuang, D. L. Voronov, and H. A. Padmore, J. Synchrotron Radiat. **21**(4), 736–743 (2014).

[17] S. G. Chiuzbăian, C. F. Hague, A. Avila, R. Delaunay, N. Jaouen, M. Sacchi, F. Polack, M. Thomasset, B. Lagarde, A. Nicolaou, S. Brignolo, C. Baumier, J. Lüning, and J.-M. Mariot, Rev. Sci. Instrum. **85**(4), 043108 (2014).

[18] H. Yamane, N. Kosugi, and T. Hatsui, J. Electron Spectrosc. Relat. Phenom. **188**, 155–160 (2013).

[19] K. D. Osborn and T. A. Callcott, Rev. Sci. Instrum. **66**(5), 3131–3136 (1995).

[20] M. C. Hettrick and J. H. Underwood, Appl. Opt. **25**(23), 4228–4231 (1986).

[21] G. Ghiringhelli, A. Piazzalunga, C. Dallera, G. Trezzi, L. Braicovich, T. Schmitt, V. N. Strocov, R. Betemps, L. Patthey, X. Wang, and M. Grioni, Rev. Sci. Instrum. **77**(11), 113108 (2006).

[22] Y.-D. Chuang, J. Pepper, W. McKinney, Z. Hussain, E. Gullikson, P. Batson, D. Qian, and M. Z. Hasan, J. Phys. Chem. Solids **66**(12), 2173–2178 (2005).

[23] C. Dallera, E. Puppin, G. Trezzi, N. Incorvaia, A. Fasana, L. Braicovich, N. B. Brookes, and J. B. Goedkoop, J. Synchrotron Radiat. **3**(5), 231–238 (1996).

[24] Y. Harada, M. Kobayashi, H. Niwa, Y. Senba, H. Ohashi, T. Tokushima, Y. Horikawa, S. Shin, and M. Oshima, Rev. Sci. Instrum. **83**(1), 013116 (2012).

[25] L. Weinhardt, O. Fuchs, A. Fleszar, M. Bär, M. Blum, M. Weigand, J. D. Denlinger, W. Yang, W. Hanke, E. Umbach, and C. Heske, Phys. Rev. B **79**(16), 165305 (2009).

[26] F. Meyer, M. Blum, A. Benkert, D. Hauschild, S. Nagarajan, R. G. Wilks, J. Andersson, W. Yang, M. Zharnikov, M. Bar, C. Heske, F. Reinert, and L. Weinhardt, J. Phys. Chem. B **118**(46), 13142–13150 (2014).

[27] L. Weinhardt, M. Blum, O. Fuchs, A. Benkert, F. Meyer, M. Bär, J. D. Denlinger, W. Yang, F. Reinert, and C. Heske, J. Electron Spectrosc. Relat. Phenom. **188**, 111–120 (2013).

[28] J. Guo, J. Electron Spectrosc. Relat. Phenom. **188**, 71–78 (2013).

[29] T. S. Arthur, P.-A. Glans, M. Matsui, R. Zhang, B. Ma, and J. Guo, Electrochem. Commun. **24**, 43–46 (2012).

[30] M. R. Howells, D. Cambie, R. M. Duarte, S. Irick, A. A. MacDowell, H. A. Padmore, T. R. Renner, S. Rah, and R. Sandler, Opt. Eng. **39**(10), 2748–2762 (2000).

[31] N. Kelez, Y.-D. Chuang, A. Smith-Baumann, K. Franck, R. Duarte, A. Lanzara, M. Z. Hasan, D. S. Dessau, T. C. Chiang, Z. X. Shen, and Z. Hussain, Nucl. Instrum. Methods Phys. Res., Sect. A **582**(1), 135–137 (2007).

[32] M. C. Hettrick, J. H. Underwood, P. J. Batson, and M. J. Eckart, Appl. Opt. **27**(2), 200–202 (1988).

[33] Y.-D. Chuang, Y.-C. Shao, A. Cruz, K. Hanzel, A. Brown, A. Frano, R. Qiao, B. Smith, E. Domning, S.-W. Huang, L. A. Wray, W.-S. Lee, Z.-X. Shen, T. P. Devereaux, J.-W. Chiou, W.-F. Pong, V. V. Yashchuk, E. Gullikson, R. Reininger, W. Yang, J. Guo, R. Duarte, and Z. Hussain, Rev. Sci. Instrum. **88**(1), 013110 (2017).

[34] M. S. Whittingham, Chem. Rev. **104**(10), 4271–4302 (2004).

[35] F. Lin, I. M. Markus, D. Nordlund, T.-C. Weng, M. D. Asta, H. L. Xin, and M. M. Doeff, Nat. Commun. **5**, 3529 (2014).

[36] J. H. Hubbell, P. N. Trehan, N. Singh, B. Chand, D. Mehta, M. L. Garg, R. R. Garg, S. Singh, and S. Puri, J. Phys. Chem. Ref. Data **23**(2), 339–364 (1994).

[37] X-Ray Data Booklet, Lawrence Berkeley National Laboratory, University of California, Berkeley, California, available at http://xdb.lbl.gov/.

[38] A. J. Achkar, T. Z. Regier, E. J. Monkman, K. M. Shen, and D. G. Hawthorn, Sci. Rep. **1**, 182 (2011).

[39] A. J. Achkar, T. Z. Regier, H. Wadati, Y. J. Kim, H. Zhang, and D. G. Hawthorn, Phys. Rev. B **83**(8), 081106 (2011).

[40] Y.-D. Chuang, Y. Shao, A. Cruz, K. Hanzel, A. Brown, A. Frano, R. Qiao, B. Smith, E. Domning, S.-W. Huang, L. A. Wray, W.-S. Lee, Z.-X. Shen, T. Devereaux, J.-W. Chiou, W.-F. Pong, V. Yashchuk, E. Gullikson, R. Reininger, W. Yang, J. Guo, R. Duarte, and Z. Hussain, "Modular soft x-ray spectrometer for applications in energy sciences and quantum materials," Rev. Sci. Instrum. **88**, 013110 (2017).

[41] J. A. Carlisle, E. L. Shirley, E. A. Hudson, L. J. Terminello, T. A. Callcott, J. J. Jia, D. L. Ederer, R. C. C. Perera, and F. J. Himpsel, Phys. Rev. Lett. **74**(7), 1234–1237 (1995).

[42] E. L. Shirley, J. Electron Spectrosc. Relat. Phenom. **110–111**, 305–321 (2000).

[43] Y. L. Chen, J. H. Chu, J. G. Analytis, Z. K. Liu, K. Igarashi, H. H. Kuo, X. L. Qi, S. K. Mo, R. G. Moore, D. H. Lu, M. Hashimoto, T. Sasagawa, S. C. Zhang, I. R. Fisher, Z. Hussain, and Z. X. Shen, Science **329**(5992), 659–662 (2010).